

Mitigating Contact Loss in $\text{Li}_6\text{PS}_5\text{Cl}$ -Based Solid-State Batteries Using a Thin Cationic Polymer Coating on NCM

Bing-Xuan Shi, Yuriy Yusim, Sudeshna Sen, Thomas Demuth, Raffael Ruess, Kerstin Volz, Anja Henss, and Felix H. Richter*

Thiophosphate-based solid-state batteries (SSBs) with high-nickel ternary cathode materials such as $\text{LiNi}_{0.83}\text{Co}_{0.11}\text{Mn}_{0.06}\text{O}_2$ (NCM) represent a promising next-generation energy storage technology due to their expected high specific discharge capacity and improved safety. However, rapid capacity fading caused by contact loss through interphase and crack formation during cell cycling is a significant problem hindering stable SSB cycling and high-energy-density applications. In this work, a uniform coating of poly((4-vinyl benzyl)trimethylammonium bis(trifluoromethanesulfonylimide)) (PVBTA-TFSI) on NCM is obtained via a spray-drying process. This exceptionally thin cationic polymer coating of only 2–4 nm thickness on NCM helps stabilize the interface between NCM and the $\text{Li}_6\text{PS}_5\text{Cl}$ solid electrolyte (SE). Electrochemical tests confirm a significant improvement in long-term cycling performance and active mass utilization compared to uncoated NCM. In addition, the polymer coating effectively suppresses the degradation of the NCM/SE interface, particularly the formation of oxygenated species, and reduces the extent of particle cracking. Overall, these results highlight a new approach to mitigate SSB degradation using a thin cationic polymer coating on NCM for SSBs.

electrochemical energy storage devices for electric vehicles and large-scale applications.^[1] In order to achieve higher energy density, intercalation-type cathode active materials and thiophosphate-based solid electrolytes have drawn much attention.^[2] High-nickel ternary $\text{LiNi}_{1-x-y}\text{Co}_x\text{Mn}_y\text{O}_2$ is a promising lithium SSB cathode active material due to its high energy density and low cost.^[3] However, severe capacity fading caused by contact loss through interface degradation and particle cracking is observed when NCM and thiophosphate-based solid electrolytes are combined in a SSB composite cathode.

In general, interface degradation between NCM and solid electrolyte creates interfacial layers that interfere with lithium-ion and electron transport. Even at a state of charge (SOC) of 0%, chemical reactions at the NCM/SE interface cause capacity fading.^[4] During the first charging process, electrochemical

degradation occurs at the NCM/SE interface due to the limited electrochemical stability window of thiophosphate-based solid electrolytes. However, the discharge process is often terminated above 2.6 V (vs Li^+/Li), preventing reduction at the NCM/SE interface during discharge. Hence, oxidation of the solid electrolyte is much slower in subsequent cycles.^[5–7]


Since the thiophosphate-based solid electrolyte is in direct contact with NCM, side reactions can occur that result in structural degradation of the surface of NCM and create a passivation layer at the NCM/SE interface. Therefore, oxygenated species such as SO_x^{n-} and PO_x^{n-} are detected by time-of-flight secondary ion mass spectrometry (ToF-SIMS) at the NCM/SE interface, and SO_2 gas is detected by differential electrochemical mass spectrometry during cycling. Oxygen loss causes mechanical cracking and plays an important role in interface degradation.^[5,8–13] Additionally, lattice contraction and expansion of NCM during cycling contributes to capacity fading.^[14–18] These degradation mechanisms have even stronger adverse effects in SSBs than in lithium-ion batteries due to contact loss between solid electrolyte and cathode active material.^[19] Consequently, research efforts are devoted to improving the stability of the electrode-electrolyte interface.

In order to enhance the interfacial stability between NCM and thiophosphate-based solid electrolyte, surface modification

1. Introduction

Lithium solid-state batteries (SSBs) using solid electrolytes (SEs) to replace organic liquid electrolytes are expected to improve battery safety and performance. They promise to be excellent

B.-X. Shi, Y. Yusim, S. Sen^[†], R. Ruess, A. Henss, F. H. Richter
Institute of Physical Chemistry & Center for Materials Research (LaMa)
Justus Liebig University Giessen
Heinrich-Buff-Ring 17, 35392 Giessen, Germany
E-mail: felix.h.richter@phys.chemie.uni-giessen.de
T. Demuth, K. Volz
Department of Physics & Materials Sciences Center (WZMW)
Philipps-University Marburg
Hans-Meerwein Straße 6, 35032 Marburg, Germany

 The ORCID identification number(s) for the author(s) of this article can be found under <https://doi.org/10.1002/aenm.202300310>

^[†]Present address: WMG, University of Warwick, Coventry CV4 7AL, UK

© 2023 The Authors. Advanced Energy Materials published by Wiley-VCH GmbH. This is an open access article under the terms of the Creative Commons Attribution License, which permits use, distribution and reproduction in any medium, provided the original work is properly cited.

DOI: 10.1002/aenm.202300310

by coating on NCM has been studied considerably. In general, wet and dry coating processes can hardly achieve a thin and uniform coating layer compared to atomic layer deposition.^[20] As a result, atomic layer deposition is often used to prepare cathode active materials with inorganic coatings such as HfO_2 .^[21] However, scaling up the production of battery materials involving an ALD coating processes remains challenging.^[22] Many research efforts focus on inorganic oxides as coating materials, such as LiNbO_3 ,^[23–25] $\text{Li}_6\text{ZnNb}_4\text{O}_{14}$,^[26] LiAlO_2 ,^[27] Li_2ZrO_3 ,^[25,28,29] $\text{Li}_4\text{Ti}_5\text{O}_{12}$,^[30] Li_3BO_3 ,^[31] and $\text{Li}_3\text{B}_{11}\text{O}_{18}$.^[28,32] In addition, halide solid electrolyte coatings, such as Li_3YCl_6 ,^[33] have been reported.

In addition, polymers can coat a substrate evenly if there is an attractive force between the functional groups of the polymer and the substrate.^[34] For instance, polyvinylpyrrolidone can act as a surfactant, modifying the surface of metal oxides.^[35] The mechanical properties of the coating material, along with its adhesion to the NCM, play a crucial role in the cathode performance during charge and discharge-induced volume changes. Polymers demonstrate great binding capability in composite cathodes. In contrast, inorganic materials, such as LiNbO_3 (Young's modulus ≈ 195 GPa), are inherently rigid and susceptible to fracture at the point contacts of NCM particles. Moreover, owing to its relatively weak binding capability, the coating material may delaminate from the NCM substrate due to contraction or cracking of NCM. On the other hand, the use of polymer-based coatings (Young's modulus ≈ 6 GPa) enables deformation and thinning, resulting in reduced cracking of coating layer and the preservation of contact between particles.^[36,37] Notably, reduced cracking may stem from decreased side reaction at the NCM/SE interface.^[10] However, a thin coating with few nanometers of thickness may not sufficiently restrict volume changes from NCM materials.^[36]

Although poly(3,4-ethylenedioxythiophene) modification on NCM and carbon additives in SSBs via molecular layer deposition has been studied,^[38] polymer coated NCMs are mostly adopted in lithium-ion batteries with liquid electrolytes.^[35,39–48] Polyelectrolytes bear ionic groups and have affinity to inorganic surfaces through strong electrostatic interactions with metal-oxide surfaces. Moreover, a polyelectrolyte with bis(trifluoromethanesulfonyl)imide counter ion has previously been used as a cathode binder in batteries with liquid electrolyte,^[49,50] implying the potential of polyelectrolytes as the promising coating material for inorganic substrates.^[51,52]

Spray drying can be classified as a wet coating method applied in industry^[53] and has successfully obtained uniform coatings on NCMs.^[36] Depending on the particle size, the spray-drying method can usually obtain two coated products. First, if particles are smaller than the drops sprayed out, the particles can be enclosed in the droplets, forming a uniform coating.^[54] Second, if the particles are more significant than the droplets, there will be many exposed parts on the surface of the particles after drying.^[55] By using Mini Spray Dryer B-290 from BUCHI, a drop of the solution is ≈ 25 μm , much bigger than the NCM particles, which are ≈ 3 – 5 μm in diameter.

Herein, we present the first polyelectrolyte coated NCM for use in solid-state batteries. Spray drying is used to obtain a uniform and thin coating of polyelectrolyte on NCM as it can be easily coated on metal oxide due to electrostatic interactions.^[51] Poly((4-vinylbenzyl)trimethylammonium

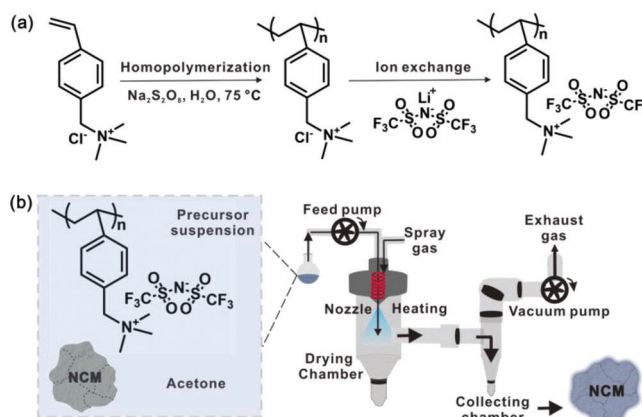


Figure 1. Schematic illustration of a) the PVBTA-TFSI synthesis and b) the process for spray coating of NCM particles, after which NCM is collected and further dried at 80 °C for 48 h in vacuum.

bis(trifluoromethanesulfonyl)imide)) (PVBTA-TFSI) is adopted as a coating material for NCM in this study. The thin PVBTA-TFSI coating on NCM significantly decreases contact loss and improves the cycling performance. We also investigate interface degradation and lithium diffusion pathway length within the cathode composite in support of the electrochemical performance results.

2. Results and Discussion

2.1. Characterization of PVBTA-TFSI Coated NCM

First, poly((4-vinylbenzyl)trimethylammonium chloride) (PVBTA-Cl) is dissolved in water solution to prepare PVBTA-TFSI through ion exchange with lithium bis(trifluoromethanesulfonyl)imide (LiTFSI). As water and alcohol solvents leach Li^+ out of NCM, these solvents must be avoided during the coating process.^[56] After ion exchange with LiTFSI, PVBTA-TFSI is soluble in acetone, which is a suitable solvent for the coating process of NCM. Since the wet-coating method often gives a non-uniform and thick coating on the surface of particles,^[20,36] the spray coating method is used here due to its possibility of obtaining a thin and uniform coating on NCM.^[36]

Figure 1 shows a schematic illustration of polymer synthesis and the spray coating processes. The polymer is synthesized through free-radical polymerization followed by anion exchange with LiTFSI. A mixture of NCM/PVBTA-TFSI/acetone is used as the precursor suspension in the spray coating process. It is sprayed out of the nozzle and is dried at a temperature of 150 °C, which is much higher than the boiling point of acetone. The polyelectrolyte coating on NCM is obtained during the drying process in the drying chamber. Finally, the dried powder is collected in the collecting chamber.^[53]

The structure of PVBTA-TFSI is confirmed by ^1H Nuclear Magnetic Resonance (^1H NMR) spectroscopy and matches the ^1H NMR spectra of the literature, as shown in Figure S1, Supporting Information.^[57] After polymerization and ion exchange, the double bonds of the monomer (^1H NMR: $\delta = 6.71, 5.82,$ and 5.26 ppm in the ^1H NMR spectra) are no longer present

in the PVBTA-TFSI spectra.^[58] Instead, a new ¹H-signal appears at 1.5 ppm, indicating that polymerization has been completed. Moreover, the aromatic protons (H3,4), benzylic protons (H5), and the protons of trimethylammonium cations (H6) still exist in the PVBTA-TFSI spectra, indicating that the polymer backbone structure is stable after ion exchange.

Figure S2, Supporting Information, shows the infrared spectra of PVBTA-Cl, and PVBTA-TFSI after anion exchange. Compared to PVBTA-Cl, PVBTA-TFSI shows new characteristic bands at 1346, 1176, 1132, and 1050 cm⁻¹, corresponding to SO₂ asymmetric stretching, CF₃ asymmetric stretching, SO₂ symmetric stretching, and S–N–S asymmetric stretching, respectively. These new peaks in the PVBTA-TFSI spectrum are attributed to TFSI anionic groups, demonstrating successful ion exchange.^[57,58] X-ray diffraction (XRD) is utilized to measure if there is any crystalline phase from LiTFSI, as shown in Figure S3, Supporting Information. The XRD pattern of PVBTA-TFSI only shows a broad, amorphous peak at ≈20°, which indicates that the PVBTA-TFSI is an amorphous polymer without residual LiTFSI separated out.

The chemical stability between PVBTA-TFSI and the solid electrolyte Li₆PS₃Cl (LPSCl) is investigated by heating a mixture of LPSCl and PVBTA-TFSI at 80 °C in a vacuum chamber for 24 h. Then the samples are examined by XRD and Fourier-transform infrared spectroscopy (FT-IR) measurements, as shown in Figure S4a,b, Supporting Information. The results indicate that PVBTA-TFSI is chemically stable with LPSCl, as the spectra are identical before and after heating. Electrochemical stability between PVBTA-TFSI and LPSCl is assessed via cyclic voltammetry, scanning from 0 to 4 V (vs Li⁺/Li-In) using a composite of vapor grown carbon fibers (VGCF) and LPSCl as the working electrode and a Li-In-alloy reference and counter electrode, as shown in Figure S5, Supporting Information. By comparing current densities between pristine and PVBTA-TFSI coated VGCF, the PVBTA-TFSI is found to have lower current density, confirming PVBTA-TFSI is electrochemically stable with LPSCl. Furthermore, the thermal stability of PVBTA-TFSI is measured by thermogravimetric analysis (TGA), as shown in Figure S6, Supporting Information. The PVBTA-TFSI decomposition temperature is ≈365 °C, and most of the decomposition happens ≈400 to 600 °C. This is much higher than the temperature applied for spray coating of NCM. The high glass transition temperature (*T_g*) of PVBTA-TFSI (74 °C) prevents softening of the polymer during cell operation, which may otherwise alter the coating layer morphology or cause deformation.^[57] In addition, the TFSI counterion increases the solubility of the polymer in acetone, which is the solvent used for spray coating, and may also help with lithium ion conduction across the coating layer, the exact mechanism of which remains unclear so far.

The microstructure of the PVBTA-TFSI coated NCM is investigated using scanning electron microscopy (SEM), as shown in Figure S7, Supporting Information. The energy selective backscattered detector and energy dispersive X-ray (EDX) detector show that 5 wt% of PVBTA-TFSI coated on NCM (5P-NCM) has some polymer particles on the surface, which can be seen distinctly in Figure S7b,c, Supporting Information. However, the 1 wt% coated NCM (1P-NCM) shows almost no polymer particles, indicating that the content of polymer needs to be sufficiently low to avoid the formation and deposition of PVBTA-

TFSI particles and ensure uniform deposition of PVBTA-TFSI on NCM. EDX analyses after focused ion beam (FIB)-cutting of coated and pristine NCM are shown in Figure S8, Supporting Information. As the fluorine signal overlaps with cobalt and the nitrogen signal is too weak to be seen even for 5P-NCM, carbon and sulfur are chosen to characterize the polymer coating. The EDX results show that the 1P-NCM has the most homogeneous coating.

The specific surface area of coated and pristine NCM is evaluated using the Brunauer–Emmett–Teller (BET) method. Pristine NCM, 1P-NCM, and 5P-NCM have a surface area of 0.593, 0.412, and 0.291 m² g⁻¹, respectively. Although SEM can hardly tell the difference in particle aggregation between pristine and PVBTA-TFSI coated NCM, the BET measurement demonstrates that the surface area decreases with the polymer coating, which may be because the polymer decreases the surface roughness.

Transmission electron microscopy (TEM) is conducted in the bright field mode using an objective aperture to enhance the contrast between the coating layer and the NCM particles. The obtained TEM images confirm that a homogenous coating layer uniformly covers all observed particles, as shown in Figure 2a–c. The 1P-NCM has a uniform coating of ≈4–6 nm in total, while the 5P-NCM has a much thicker coating layer of ≈10 nm in total. Moreover, some places of 5P-NCM even show localized polymer aggregation with a thickness of 40–100 nm (Figure S9, Supporting Information), which matches with the SEM results in Figure S7b,c, Supporting Information. Unexpectedly, a 2–4 nm thick surface layer is also observed on the pristine NCM. However, this coating layer is thinner than the polymer coatings on the 1P-NCM and 5P-NCM. Therefore, 1P-NCM has the most uniform polymer coating of ≈2–4 nm thickness, and 5P-NCM has a polymer coating of ≈8 nm thickness with some polymer aggregation.

In order to characterize the coating composition and its distribution even more precisely, ToF-SIMS measurements are carried out as a technique with high surface sensitivity. To identify chemically the coating on the NCM particle structure, a pressed pellet of PVBTA-TFSI powder is measured as a reference material. Because of the collision cascade initiated by the highly energetic analysis, beam charged fragments such as CH₂OF⁻, SNO⁻ and CF₃⁻ are formed during the ToF-SIMS measurement with a decent signal intensity (Figure 2d). As shown in Figure 2d, these fragments are also formed at the coated samples, confirming that the PVBTA-TFSI coating is present on the NCM particles. Interestingly, the intensities of the coating signals are higher for the 5P-NCM than for the 1P-NCM. This is in good agreement with the SEM and TEM results, which show that the 5P-NCM coating is thicker and more aggregated on the surface, resulting in higher signal intensity during ToF-SIMS measurements. In this context, it should be noted that due to the matrix effect^[59] the intensities of the pristine PVBTA-TFSI polymer (reference material) cannot be compared with coated NCM samples.

In addition, the ToF-SIMS depth profiles in Figure S10, Supporting Information, show that the SNO⁻ signal decreases and the NiO₂⁻ signal increases faster for the 1P-NCM than for the 5P-NCM. This confirms that the 5 wt% coating is thicker than the 1 wt% coating. Moreover, ToF-SIMS images of the SNO⁻ signal (representing the polyelectrolyte coating) in Figure 2e validate that the coatings are distributed uniformly on the surface of the

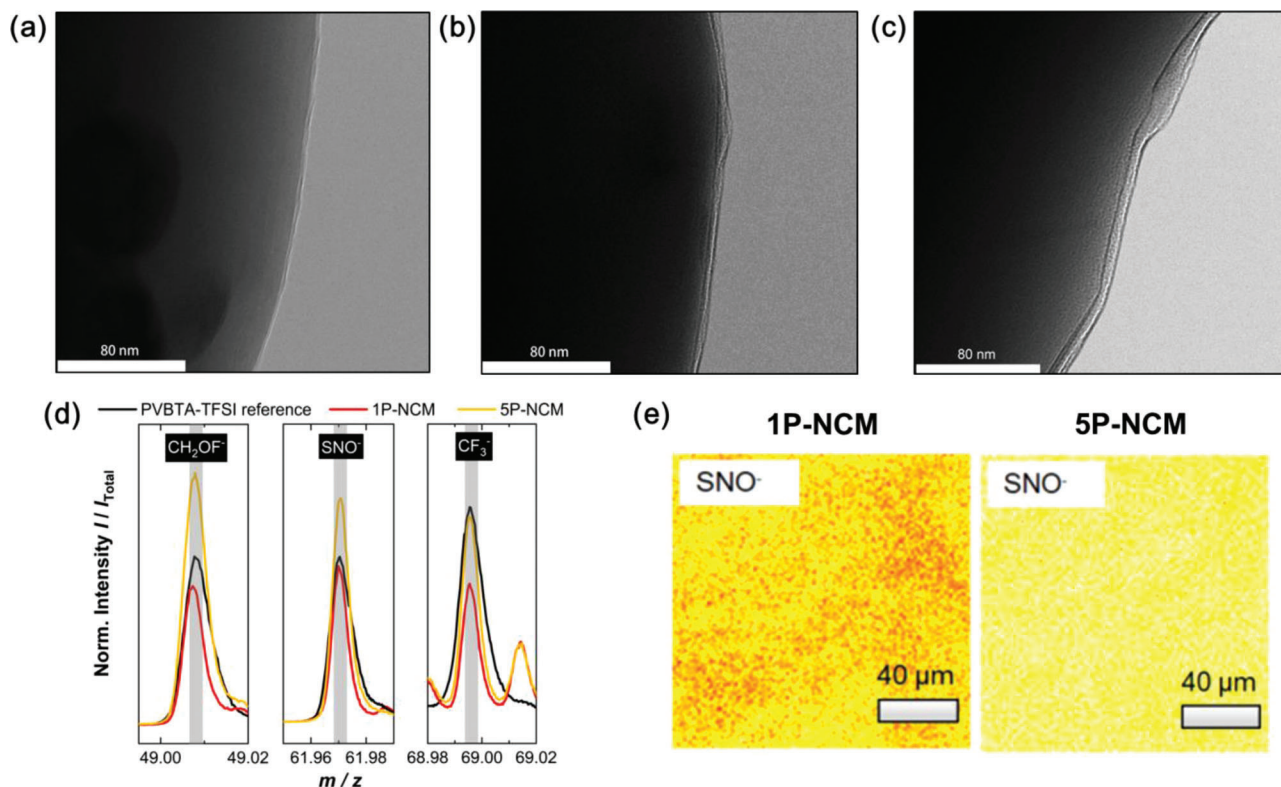


Figure 2. TEM images of a) pristine NCM, b) 1P-NCM, and c) 5P-NCM. These show that 1P-NCM has a 2–4 nm polymer coating layer covering the particles. However, 5P-NCM has a much thicker polymer coating layer of ≈ 8 nm. d) ToF-SIMS data of PVBTA-TFSI reference, 1P-NCM and 5P-NCM for CH₂OF⁻, SNO⁻, and CF₃⁻ fragments. e) ToF-SIMS mappings for the SNO⁻ fragment (representative of the polyelectrolyte coating) of 1P-NCM and 5P-NCM. ToF-SIMS evaluation confirms a homogenous PVBTA-TFSI coating on NCM.

NCM, which is consistent with the SEM and TEM results shown above.

In summary, taking the SEM, TEM, and ToF-SIMS results into account, the PVBTA-TFSI coating microstructure can be described as follows. The coating is distributed uniformly and covers the NCM particles. Furthermore, while the 1 wt% polymer coating is 2–4 nm thick, the 5 wt% polymer coating is thicker (8 nm) and has localized polymer aggregation with a thickness of 40–100 nm on the surface. Based on these analytical results, both coatings are expected to prevent direct physical contact between NCM and SE and stabilize the interface. The coating thickness of 1P-NCM matches with the best results of the poly(3,4-ethylenedioxythiophene) coating thickness (5 nm) on NCM published by Deng et al.^[38]

2.2. Rate Capability Test

The performance of the coated NCMs is compared to that of the commercially obtained pristine NCM through rate capability and cycling stability tests in SSBs made of NCM, LPSCl and a lithium-indium alloy anode. Rate capability is investigated by running five cycles for each current density (0.1, 0.25, 0.5, and 1 C), as shown in **Figure 3a**. Initially, 1P-NCM and 5P-NCM do not perform better than pristine NCM. However, 5P-NCM and pristine NCM cells have similar performance at 0.5 and 1 C, but the capacity of 1P-NCM is 4% and 11.7% higher than pristine NCM at

0.5 and 1 C, respectively. The reasons that 1P-NCM exhibited better performance than the 5P-NCM and pristine NCM cells at 0.5 and 1 C might be due to the protection of polymer coating after several cycles or the effect of protection may be more pronounced at higher C-rates. Another possibility is that reduced crack formation of 1P-NCM, coupled with an optimal polymer content that does not cause insulation, leads to better performance at higher C-rates. However, the advantages conferred by the reduced crack formation are less pronounced at lower current density. Additionally, at the 25th cycle, the coated NCM shows better reversibility in the discharge process, as shown in **Figure S11b**, Supporting Information.

Figure 3b magnifies the galvanostatic charging profile from 2 to 3 V (vs Li⁺/Li-In) in differential form for the first charge cycle. The area below 3 V in the dQ/dE diagram of pristine NCM is higher than that of 1P-NCM and 5P-NCM, respectively. This demonstrates that 5P-NCM and 1P-NCM have less electrochemical degradation at the NCM/SE interface than pristine NCM below 3 V, and this effect is the most significant in the first cycle.^[60] However, the protective layer gives rise to a larger overpotential at ≈ 3 V (vs Li⁺/Li-In) for the coated cells compared to the pristine cell in the first cycle, as shown in **Figure S11a**, Supporting Information. Overall, the 1P-NCM has the best performance compared to pristine NCM and 5P-NCM at 0.5 and 1 C. It is evident that the polymer coating reduces the electrochemical degradation below 3 V but increases the overpotential.

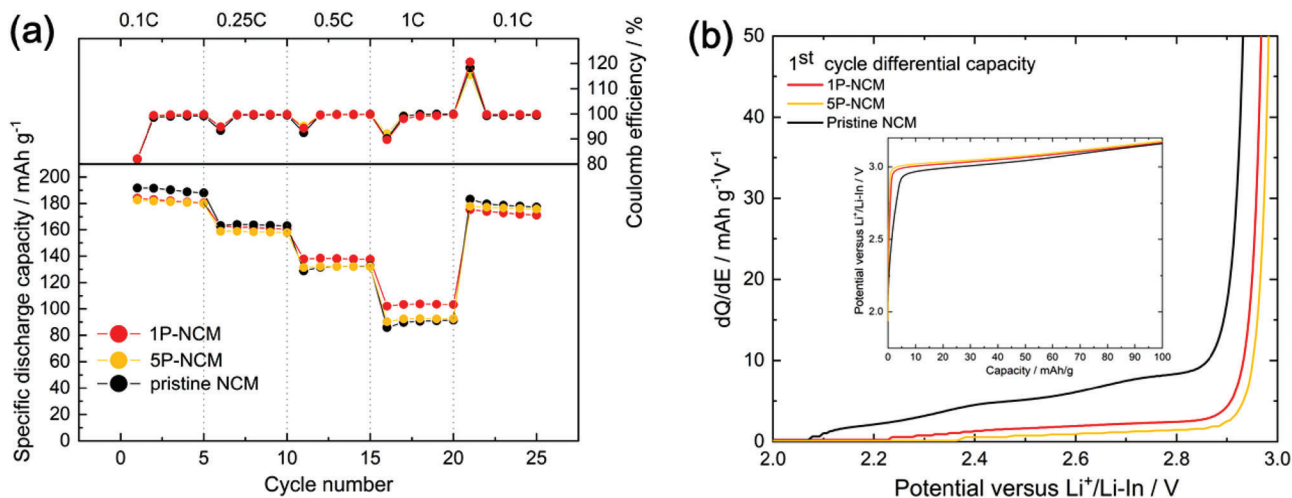


Figure 3. a) Rate capability tests of SSBs with lithium-indium alloy anode, LPSCl and pristine NCM, 1P-NCM, or 5P-NCM by testing different C-rates for 5 cycles each (0.1, 0.25, 0.5, 1, and then back to 0.1 C). The capacity under 0.5 and 1 C confirms the better rate capability for 1P-NCM. b) The differential capacity plot of the first cycle of the galvanostatic charging profile at 0.1 C is shown together with an enlargement from 2 to 3 V (vs Li⁺/Li-In), and the inset shows the corresponding galvanostatic charging profiles. The lower differential capacity for 1P-NCM and 5P-NCM indicate less electrochemical degradation for coated NCM below 3 V (vs Li⁺/Li-In).

2.3. Cycling Performance

In order to observe the influence of the PVBTa-TFSI coating layer on battery performance, 5P-NCM, 1P-NCM, and pristine NCM cells are galvanostatically cycled at 0.1 C (Figure 4a) and 0.25 C (Figure S12a, Supporting Information). At 0.1 C cycling (Figure 4a), the capacity retention of 1P-NCM is highest with 86% and that of 5P-NCM is about 75%. However, the capacity retention of pristine NCM is only $\approx 70\%$. This ranking is corroborated by the 0.25 C cycling performance (Figure S12a, Supporting Information). Therefore, 1P-NCM significantly improves the long-term cycling stability of NCM in SSBs with LPSCl.

The improved cycling performance of the SSBs with polyelectrolyte coated NCM can be caused by several reasons. For one, avoiding the electrochemically inactive interfacial layer between the active material and the electrolyte leads to higher active mass utilization of the cathode material.^[8,61] Here, the active mass means the actual amount of active material utilized in the reaction. Interface decomposition between the active material and the electrolyte includes chemical,^[4] electrochemical,^[5-7] and chemo-mechanical degradation reactions.^[5,8-13] This may form an electrochemically inactive interface, a high resistance interlayer and chemo-mechanical contraction,^[62,63] all of which can cause a loss of contact between the NCM and the solid electrolyte, leading to increased cathode composite resistance (R_{cathode}).^[64] For another, the improvement could be caused by preventing an increase of the lithium diffusion pathway.^[8] Lithium diffusion pathway length may increase due to internal particle cracking,^[14,15,17,19,65] contact loss, and interface decomposition as listed above.^[8]

2.4. Contact Loss and Electrochemically Inactive Interfacial Layer

In this study, contact loss applies to both the formation of an electrochemically inactive interfacial layer and physical separation between the NCM and LPSCl electrodes. Both reduce the

effective contact area of NCM/LPSCl during cycling, resulting in active mass loss and higher interface resistance. We summarize these two degradation mechanisms here using the term contact loss, as their influence on ion transport and cell performance is comparable and they are hard to distinguish experimentally. In order to quantify and analyze the extent of contact loss, the active mass and interfacial resistance in operating cells are measured during the cycling test. The impedance test is performed at 3.15 V (vs Li⁺/Li-In) under the current of 0.1 C at specific cycles. The potential of 3.15 V (vs Li⁺/Li-In) is chosen to ensure a sufficiently high lithium diffusion coefficient and lowest R_{cathode} while avoiding significant degradation during the measurement. Moreover, the layered oxide cathode material impedance depends on the electrode's SOC, so it is necessary to measure the impedance at a fixed potential.^[66]

Chronoamperometry is used right before electrochemical impedance spectroscopy (EIS) to ensure that the impedance can be measured at a sufficiently steady state. The cell voltage is stabilized at 3.15 V (vs Li⁺/Li-In) until the current drops to less than 1%. This allows Li⁺ diffusion within the NCM particles and dissipates the lithium concentration gradient within.^[8,27,30] After crack formation in NCM particles, unlike liquid electrolytes, SEs cannot infiltrate these cracks. Therefore, while contact loss can change the interface resistance, the impact of particle crack formation is stronger on the lithium diffusion process within the NCM particles than on the charge transfer at the interface.^[19]

Additionally, 2 h of relaxation time is used to record the open circuit potential (V_{OC}) after every charging and discharging process to calculate the active mass.^[8] Briefly, a cell made of NCM cathode and lithium-indium alloy anode with a fixed potential has an equilibrium V_{OC} . The V_{OC} follows a well-defined function versus SOC representing lithium content (x in $\text{Li}_x\text{Ni}_{0.83}\text{Mn}_{0.06}\text{Co}_{0.11}\text{O}_2$) of NCM. Using the reference data of the V_{OC} function with x in $\text{Li}_x\text{Ni}_{0.83}\text{Mn}_{0.06}\text{Co}_{0.11}\text{O}_2$ (Figure S13, Supporting Information), the actual specific capacity (Q_{act}) can be determined by the difference in SOC after the charging and

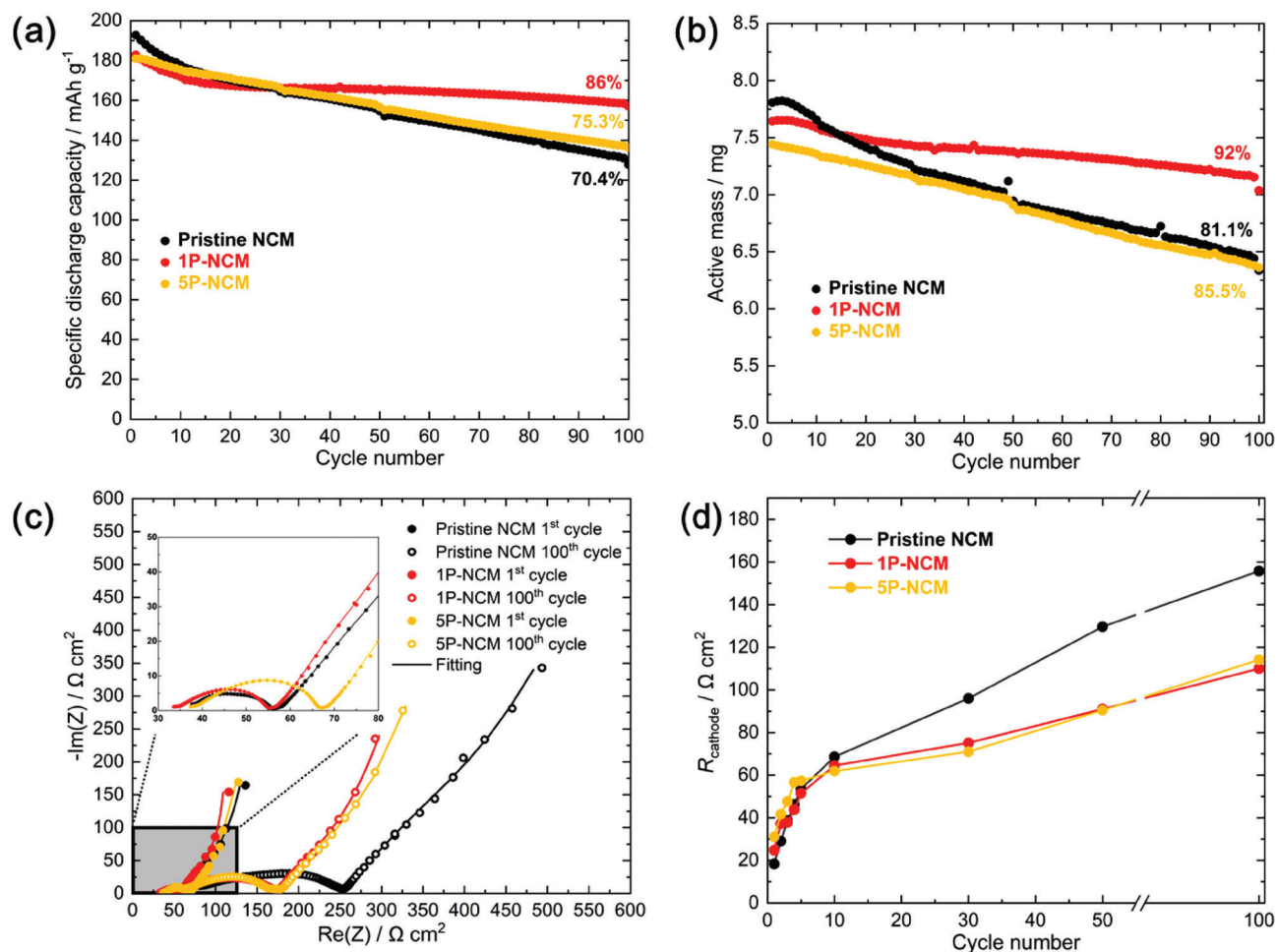


Figure 4. a) Long-term cycling capability of SSBs with lithium-indium alloy anode, LPSCI and pristine NCM, 1P-NCM, or 5P-NCM at 0.1 C, b) corresponding active mass evolution, c) Nyquist plot for first and 100th cycle, and d) R_{cathode} versus cycles of polymer coated NCM and pristine NCM are compared. The impedance results and active mass calculations confirm that the polymer coating can effectively alleviate the contact loss and electrochemically inactive interfacial layer.

discharging process. Then the active mass (m_{act}) can be calculated by the measured discharge capacity (Q_{meas}) and Q_{act} in the following equation (Equation (1)).

$$m_{\text{act}} = \frac{Q_{\text{meas}}}{Q_{\text{act}}} \quad (1)$$

The m_{act} of PVBTA-TFSI coated NCM cells and pristine NCM cells of the 0.1 C cycling test are compared in Figure 4b. The actual mass of NCM in the electrodes is set to be 8.3 mg. Initially, 1P-NCM, 5P-NCM, and pristine NCM cells have a determined m_{act} of ≈ 7.6 , 7.4, and 7.8 mg, respectively. This means that in the first cycle, the m_{act} for 1P-NCM and 5P-NCM is slightly less than for the pristine NCM due to polymer coating or polymer aggregation on NCM. However, after 100 cycles at 0.1 C, the retention of m_{act} of pristine, 1P-NCM, and 5P-NCM cells are $\approx 81\%$, 92%, and 86%, respectively. The better m_{act} retention for PVBTA-TFSI coated NCM cells during cycling is explained as the alleviation of contact loss caused by interface degradation. Nevertheless, 1P-NCM shows better m_{act} retention than 5P-NCM as the polymer

coating layer of 5P-NCM is probably too thick, hindering charge transfer and electronic and ionic transport. Similar results can also be observed in the 0.25 C cycling test (Figure S12b, Supporting Information).

It is worth noting that the m_{act} of pristine and coated NCMs all show a close to linear decrease during cycling (Figure 4b). However, the capacity of pristine NCM and 1P-NCM has rapidly decayed in the beginning, and the capacity of 5P-NCM has a close to linear decay (Figure 4a). Therefore, it can be concluded that the rapid capacity decay for pristine NCM and 1P-NCM compared to 5P-NCM before the 30th cycle may be due to more severe mechanical degradation, such as particle cracking. In the early stages ($\approx 30^{\text{th}}$ cycles), 5P-NCM exhibits slower capacity degradation than pristine NCM and 1P-NCM. This improvement is attributed to the cohesive influence of the 5 wt% polymer coating, which effectively stabilizes the electrode. However, too much polymer content increases the lithium diffusion pathway length, reducing the capacity to less than 1P-NCM after 100 cycles. On the other hand, the m_{act} results are not as affected by the particle cracking within the NCM, but are more affected by the

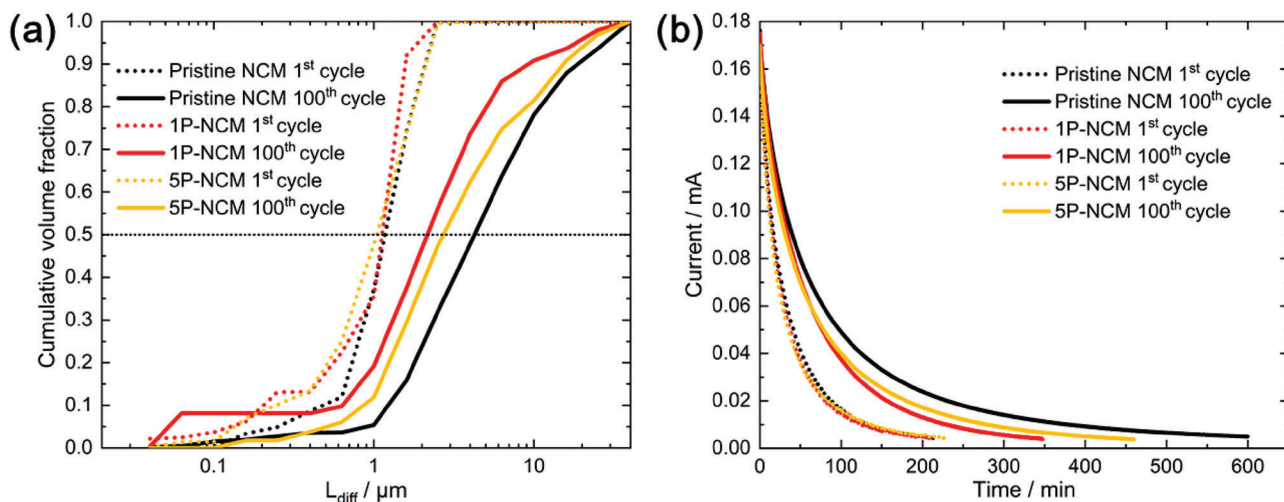


Figure 5. a) Evolution of the lithium diffusion pathway length (L_{diff}) estimated using the EIS-PSD model. The EIS-PSD model fits the Warburg impedance to obtain the cumulative volume fraction of particle sizes, representing lithium diffusion pathway length. b) The chronoamperometry measurement shows the time it takes for the current to drop to less than 1% of charging current, which is indicative of the lithium diffusion pathway length. The results of the EIS-PSD model and chronoamperometry measurement demonstrate that the polymer coating can lessen the length increase of the lithium diffusion pathways during cycling.

contact loss and interface degradation, giving rise to a constant linear decay.

EIS measurements of 0.1 C are carried out during cycling, as shown in Figure 4c,d. The transition line model is used for fitting. Additionally, the transition line model and fitting results are described in Figure S14 and Table S1, Supporting Information, respectively.^[67] The interface between the cathode and the solid electrolyte is an essential factor affecting cathode resistance (R_{cathode}), providing information on contact loss and interface degradation. The cathode composite resistance R_{cathode} is expressed as the geometric mean of the value charge transfer resistance (R_{ct}) multiplied by the sum of the electronic resistance (R_{ele}) and ionic resistance of electrolyte in the cathode composite (R_{ion}) (see Figure S14, Supporting Information).^[67]

In the first cycle at 3.15 V (vs $\text{Li}^+/\text{Li-In}$), a thicker polymer coating layer gives rise to a higher R_{cathode} (pristine NCM: $18.3 \Omega \text{ cm}^2$, 1P-NCM: $24.8 \Omega \text{ cm}^2$, 5P-NCM: $31.1 \Omega \text{ cm}^2$), matching the first cycle m_{act} results mentioned above, as a thicker polymer coating layer gives rise to lower m_{act} . Nonetheless, the R_{cathode} of the pristine NCM cell increases more significantly after 100 cycles than that of 1P-NCM and 5P-NCM cells (pristine NCM: $155.8 \Omega \text{ cm}^2$, 1P-NCM: $110.4 \Omega \text{ cm}^2$, 5P-NCM: $114.2 \Omega \text{ cm}^2$). Although R_{cathode} of pristine NCM shows a 1.4 times higher value than that of 5P-NCM after 100 cycles, the retention of the 5P-NCM is 5% more than that of pristine NCM, and the capacity is also higher (the capacity of 5P-NCM is $\approx 10 \text{ mAh g}^{-1}$ more than that of pristine NCM). The significant increase in the R_{cathode} of the pristine NCM cell may be caused by severe interface degradation. Additionally, 1P-NCM and 5P-NCM cells have similar R_{cathode} after 100 cycles, indicating that 1 wt% of the polymer coating layer is sufficient to act as a protective layer for NCM.

However, although the R_{cathode} of 5P-NCM and 1P-NCM are similar, the observed difference in discharge capacity is attributed to the high polymer content in 5P-NCM. This excess polymer increases the lithium diffusion pathway length (see Figure 5),

reducing the capacity below 1P-NCM after 100 cycles. The EIS measurements for 0.25 C cycling cells (Figure S12c, Supporting Information) also show the same conclusion as the 0.1 C results. Overall, EIS measurements and m_{act} calculations indicate that the polymer coating can act as a protective layer, alleviating contact loss at the NCM/LPSCl interface.

2.5. Lithium Diffusion Pathways within the Cathode Composite

The loss of m_{act} causes an irreversible capacity fading that increases with the number of charge–discharge cycles. In addition, the lithium diffusion pathway length also affects capacity fade. The lithium diffusion pathway length within the cathode composite is expected to increase during cycling due to contact loss, interface degradation, and NCM particle cracking. Warburg impedance in EIS is fitted using the particle size distribution (EIS-PSD) model reported in our previous study to determine the length of the lithium diffusion pathway within the cathode composite.^[8]

In general, the ideal finite-space Warburg impedance describes the diffusion throughout the sample volume, including the ion-blocking boundary at the current collector and the innermost center of the NCM particles. If the frequency is low enough to access the blocking boundary, the impedance shows a continuous transition from 45° to 90° in the Nyquist plot.^[68] Consequently, to measure the finite-space Warburg impedance in EIS, the lower cut-off frequency is set to 100 μHz . The finite-space Warburg impedance element of cylindrical particles ($Z_{\text{fs}}^{\text{cylindrical}}$) is used to describe the complex geometry of Li^+ diffusion in the NCM by fitting the finite space diffusion tail of EIS coupled with the transition line model, as shown in Figure S14, Supporting Information.

$$\tau_i = L_{\text{diff}}^2 / \bar{D}_{\text{Li}} \quad (2)$$

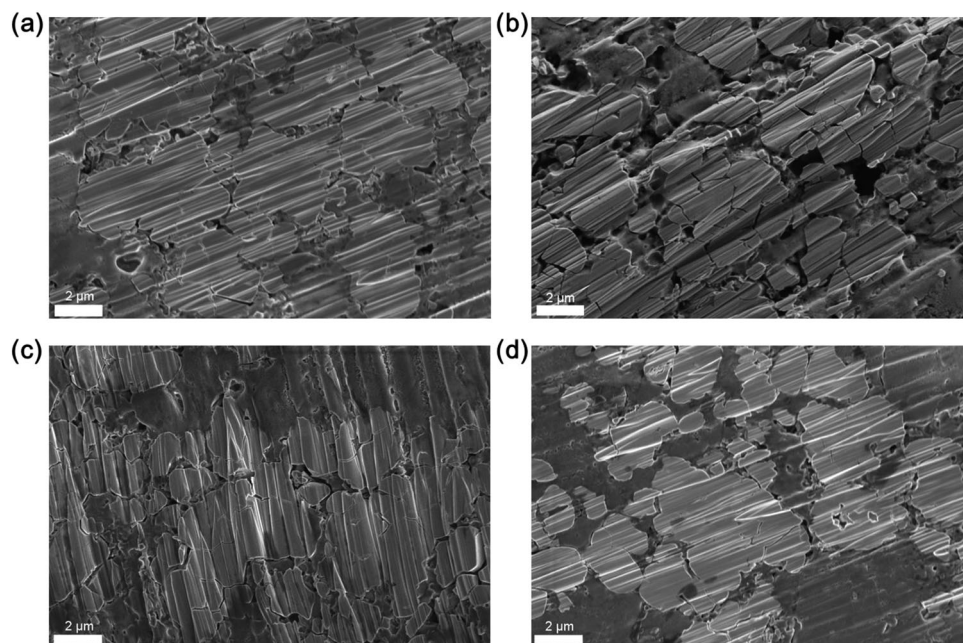


Figure 6. FIB-SEM images of cathode composites after 200 cycles at 0.25 C. Pristine NCM a) before and b) after cycling shows a big difference in NCM particle cracking. The cracking within the pristine NCM cathode happens severely after cycling. However, c) 1P-NCM and d) 5P-NCM cells after cycling show less cracking compared to pristine NCM after cycling.

and

$$Z_{fs}^{\text{cylindrical}} = \frac{1}{C_{\text{diff}}} \left(\sum_i \frac{\Delta Q_i}{\tau_i} \frac{\sqrt{i\omega\tau_i}}{\coth \sqrt{i\omega\tau_i}} \right)$$

The $Z_{fs}^{\text{cylindrical}}$ is dependent on the characteristic time constant of lithium diffusion τ_i (Equation (2))^[69] and the volume fraction of particle contribution ΔQ_i (Equation (3)).^[8] C_{diff} is the total differential capacity of the entire electrode ($C_{\text{diff}} = \partial Q / \partial E = 340 \frac{\text{mAh}}{\text{Vg}}$), and calculated from the reference data at 3.15 V (vs $\text{Li}^+/\text{Li-In}$), which equals about 3.77 V (vs Li^+/Li), and $x = 0.6$ (Figure S13, Supporting Information). \tilde{D}_{Li} is the chemical diffusion coefficient of lithium and is assumed as $10^{-11} \text{ cm}^2 \text{ S}^{-1}$ at 25 °C, cited from our previous study and obtained by the fitting of the semi-finite part of the diffusion tail in EIS.^[8] ω is the radial frequency. The thickness of the cylindrical particle (L_{diff}) in Equation (2) can be taken as the lithium diffusion pathway length. Therefore, if the lithium diffusion pathway length increases due to internal particle cracking, the finite-space Warburg impedance overestimates particle size.

Fitting of the impedance measurement yields L_{diff} values and the volume fractions (represented in a cumulative form) are shown in Figure 5a. It can be seen that L_{diff} of pristine NCM increases considerably (from ≈ 1.1 to $4.3 \mu\text{m}$) compared to 1P-NCM (from ≈ 1.0 to $2.2 \mu\text{m}$) and 5P-NCM (from ≈ 1.0 to $2.7 \mu\text{m}$). This indicates that particle cracking is less severe for the PVBTa-TFSI coated NCM.

The results of chronoamperometry (Figure 5b) indicate the same conclusion. The time it takes for the current to drop to less than 1% of charging current is related to the lithium diffusion pathway length, that is, the longer the time, the longer the

lithium diffusion pathway length.^[70] Figure 5b shows that at the 100th cycle of 0.1 C cycling, the pristine NCM cell needs 600 min. However, 5P-NCM and 1P-NCM cells need only 460 and 347 min, respectively. Additionally, chronoamperometry results for 0.25 C cycling give the same trends as for 0.1 C, as shown in Figure S15, Supporting Information.

Despite similar R_{cathode} values for 5P-NCM and 1P-NCM (refer to Figure 5), the discharge capacity difference after 100 cycles is due to the increased lithium diffusion pathway length, resulting in a reduced capacity for 5P-NCM compared to 1P-NCM. In addition, as the primary ion-conduction path occurs through interconnected LPSCl particles in the cathode composite, excess polymer may partially obstruct the lithium diffusion pathway.^[71] Similar capacity degradation difference is also observed when increasing binder content to $\approx 4\%$ in SSBs with NCM composite cathode and LPSCl electrolyte using ethyl cellulose as a binder.^[72] Overall, the chronoamperometry and EIS-PSD calculation results indicate that after cycling the pristine NCM cell has a much longer lithium diffusion pathway length than the coated NCM cells.

2.6. Particle Cracking after Cycling

FIB-SEM is employed to observe the morphological change of the cross-section in the cathode composite after 200 cycles at 0.25 C, as shown in Figure 6. The pristine NCM cell shows more fracture lines within the particles than the 1P-NCM and 5P-NCM cells, and the 5P-NCM cells have the least cracking. One of the reasons for alleviating cracking may be due to the less lithium extracted from the NCM, especially for the second hexagonal phase to the third hexagonal phase (H2 + H3) transition during the charging

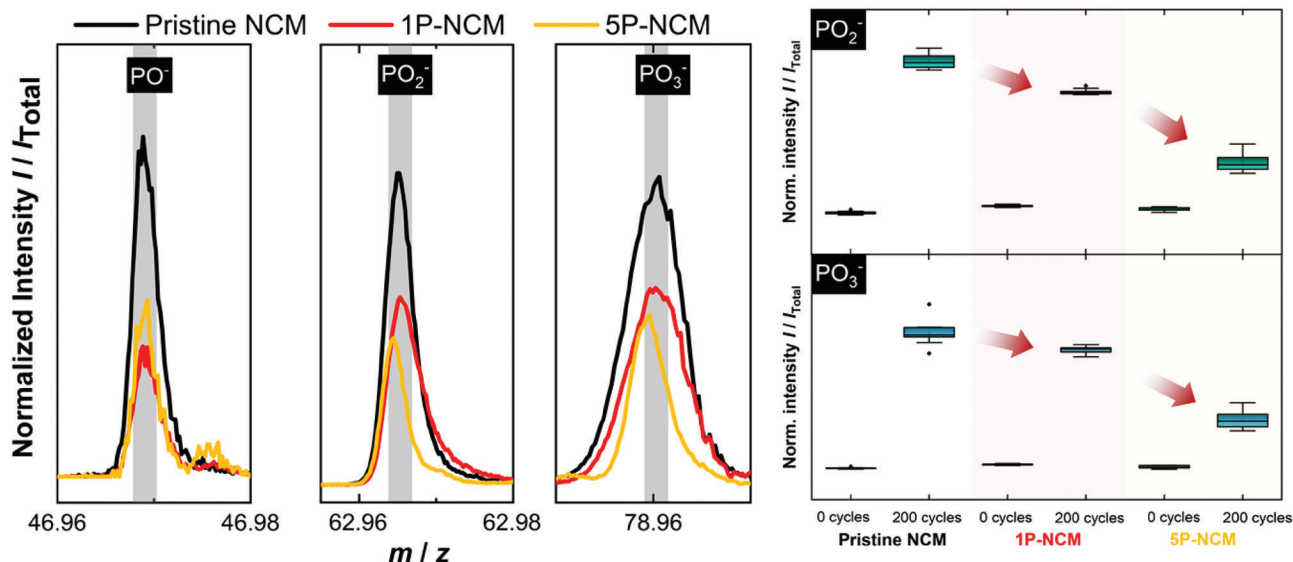


Figure 7. a) ToF-SIMS mass spectra for fragments that can be assigned to oxidative interfacial decomposition products such as PO^- , PO_2^- , and PO_3^- for pristine NCM, 1P-NCM, and 5P-NCM after 200 cycles. b) Corresponding boxplots of normalized intensities for PO_2^- and PO_3^- signals containing ten data points each. The 1P-NCM and 5P-NCM suppress the formation of oxidative decomposition products compared to the pristine NCM.

step, which has the most severe volume change.^[73] However, the capacity (Figure S16, Supporting Information) and the area under the dQ/dE plot (Figure S11, Supporting Information) above 3.48 V (vs $\text{Li}^+/\text{Li-In}$), which is ≈ 4.1 V (vs Li^+/Li), is similar for both PVBTA-TFSI coated NCM cells and the pristine NCM cell in the first cycle charging step, indicating that all the NCM cells have similar H2+H3 phase transition processes. Moreover, as noted in section 2.5 (Figure 5), pristine NCM has the longest lithium diffusion pathway length, which is typically caused by particle cracking within the NCM, which matches with the low-angle FIB SEM results after cycling. It is likely that a thin coating with just a few nanometers is insufficient to inhibit fully the volume changes occurring in CAM materials. However, the NCM particle cracking may be alleviated because the polymer can reduce side reaction at the NCM/SE interface during cycling.^[10]

2.7. Interfacial Stability after Cycling

ToF-SIMS analysis is carried out to identify decomposition products and to reveal the influence of the NCM coatings on degradation processes due to electrochemical cycling. In contrast to XPS, ToF-SIMS allows the detection of small amounts of interfacial decomposition products such as phosphates, which was demonstrated in detail by Walther et al.^[11,23,74] In this work, we analyze composite cathodes with 1P-NCM and 5P-NCM and compare the results with data obtained for composite cathodes with pristine NCM.

In this context, the samples are analyzed before cycling and after 200 cycles, in line with the study by Walther et al.^[23] As described by Walther et al., three different decomposition processes (current collector/solid electrolyte, carbon additive/solid electrolyte, NCM/solid electrolyte) must be considered. A good indication for oxidative decomposition processes of the solid electrolyte can be obtained by surface analysis of the composite

cathode after removal of the stainless-steel current collector. Thereby, it should be mentioned that surface spectra lead to comparable results as depth profiling.

According to previous studies with ToF-SIMS, phosphate (PO_x^-) and sulfate/sulfite (SO_x^-) fragments are of particular interest to evaluate decomposition processes in thiophosphate-based composite cathodes due to electrochemical cycling.^[11,23,74] However, since the PVBTA-TFSI coating in this work contains SO_2 -groups, the analysis of sulfate/sulfite fragments may lead to misinterpretations. Thus, only phosphates are considered in the following analysis. In addition, a quantification of the degradation products is not possible with ToF-SIMS, since it is a semi-quantitative method (signal intensity is not only proportional to the concentration of the species). Thus, no y-axis values are shown in the images.^[75]

A direct comparison of the mass spectra normalized to the total intensity after 0.25 C cycling (200 cycles) is exemplarily shown in Figure 7a. It can be seen that the amount of PO_x^- fragments, in particular PO^- , PO_2^- , and PO_3^- , is significantly higher for the uncoated sample than for the coated samples, which indicates that the 1 wt% and 5 wt% PVBTA-TFSI coatings suppress the formation of phosphates. Accordingly, the decomposition of the thiophosphate-based solid electrolyte is inhibited by the protective function of the PVBTA-TFSI coating since the direct physical contact between NCM and solid electrolyte is reduced. Furthermore, it can be seen that the amount of PO_2^- and PO_3^- fragments is higher for the 1P-NCM than for 5P-NCM. This indicates that the thicker 5 wt% coating is more effective in suppressing the decomposition of the solid electrolyte than the thinner 1 wt% coating. However, it can be seen that this trend is not valid for the PO^- signal, which could be due to mass interferences with the CCl^- signal that is already present in the composite cathode before cycling.

To ensure sufficient statistical sampling and reliability of the results, 10 mass spectra per sample were measured before and

after cycling. These are plotted in boxplots to semi-quantitatively compare normalized fragment intensities for the PO_2^- and PO_3^- fragments (see Figure 7b). It can be seen that the trend of having less decomposition products in the composite cathodes with coated NCM is confirmed. However, oxidative decomposition products can still be detected, which may form at the unprotected interface between the carbon additives and the solid electrolyte.

Overall, the comparison of oxidative decomposition products by ToF-SIMS confirms that PVBTA-TFSI coating significantly improves the interfacial stability at the NCM/SE interface in comparison to pristine, uncoated NCM. This supports the electrochemical data shown above. The present study demonstrates that polymers can act as suitable coating on NCM for use in solid-state batteries. Nevertheless, further investigation into the property-performance relationship is required, particularly regarding the significance of the polymer functional groups, charge and chemical nature of the counterion. Such dedicated investigations are expected to provide deeper insight into the structure-property relationship of polymer coatings in the near future.

3. Conclusion

This study presents a new approach to improve the cycling stability in SSB cathodes using an exceptionally thin cationic polymer coating on NCM. The PVBTA-TFSI polymer is synthesized by free-radical polymerization and ion exchange. It is applied as a coating on NCM by spray drying. TEM and ToF-SIMS measurements show that the spray drying method affords a uniform and thin polymer coating of only 2 nm to 4 nm thickness around the NCM particles by adding ≈ 1 wt% of polymer. The PVBTA-TFSI coated NCM exhibits better capacity retention and better active mass retention than the corresponding SSB cells with pristine NCM. In addition, the increase of the lithium diffusion pathway length during cycling is mitigated by the polymer coating, which is confirmed by chronoamperometry and EIS-PSD fitting. FIB-SEM after cycling shows that the polymer coating reduces the extent of particle cracking within NCM. Thus, the presented polymer coating mitigates several typical degradation mechanisms in $\text{Li}_6\text{PS}_5\text{Cl}$ -based SSB cathodes.

4. Experimental Section

Reagents and Materials: (Vinylbenzyl)trimethylammonium chloride (VBTA-Cl) monomer, reagent grade sodium persulfate ($\text{Na}_2\text{S}_2\text{O}_8$) initiator, lithium bis(trifluoromethanesulfonyl)imide (LiTFSI), and vapor-grown carbon fibers (VGCF) were purchased from Sigma-Aldrich. Single crystal high-nickel $\text{LiNi}_{0.83}\text{Co}_{0.11}\text{Mn}_{0.06}\text{O}_2$ (NCM) was purchased from MSE Supplies (particle size ≈ 3 – 5 μm , and BET specific surface area ≈ 0.5 – 0.9 m^2 g^{-1}). $\text{Li}_6\text{PS}_5\text{Cl}$ (LPSCI) was purchased from NEI Corporation. Indium foil was purchased from chemPUR GmbH with 100 μm thickness and punched into a circular electrode of 9 mm in diameter. Lithium foil was purchased from Albemarle Rockwood Lithium GmbH with 125 μm thickness and punched into a circular electrode of 6 mm in diameter.

Synthesis of PVBTA-TFSI: Poly((4-vinylbenzyl)trimethylammonium bis(trifluoromethanesulfonyl)imide) was synthesized through the route shown in Figure 1. First, free radical polymerization was conducted by mixing 5 g VBTA-Cl and 0.3 mL of saturated $\text{Na}_2\text{S}_2\text{O}_8$ solution in 20 mL of deionized water and then heated up and purged with N_2 flow at 75 $^\circ\text{C}$ for 48 h (molar ratio of VBTA-Cl: $\text{Na}_2\text{S}_2\text{O}_8 = 1:0.3$). After polymerization,

PVBTA-Cl was purified by dialysis with a considerable amount of deionized water and further condensed by a rotary evaporator.

The condensed polymer solution was then added dropwise to the LiTFSI solution (7.5 g of LiTFSI dissolved in 20 g of deionized water) and stirred overnight for ion exchange. Once the PVBTA-Cl drops into the LiTFSI solution, the PVBTA-TFSI precipitates immediately. After ion exchange, PVBTA-TFSI was washed with deionized water by centrifuge three times to remove residual salts. Thereafter, PVBTA-TFSI was dried in a vacuum oven at 80 $^\circ\text{C}$ for 72 h and stored in the glove box.

^1H NMR (400 MHz, deuterated acetone): δ 1.36–1.99 (H1, H2), δ 2.05 (acetone- d_6), δ 3.14 (H6), δ 4.4–4.9 (H5), and δ 6.5–7.4 (H3, H4). FT-IR of PVBTA-TFSI (cm^{-1}): 973 (C–N stretching), 1346, 1326, 1176, 1132, 1050 (TFSI $^-$), 1612, 1480, 1422 (aromatic C=C stretching), and 3043, 2922, 2852 (alkyl C–H stretching), 3400 (H_2O). FT-IR of PVBTA-Cl (cm^{-1}): 973 (C–N stretching), 1612, 1480, 1422 (aromatic C=C stretching), and 3015, 2922, 2852 (alkyl C–H stretching), 3400 (H_2O). FT-IR of LiTFSI (cm^{-1}): 1327 (SO_2 asymmetric stretching), 1245 (CF_3 symmetric stretching), 1204 (CF_3 asymmetric stretching), 1147 (SO_2 symmetric stretching), and 1065 (asymmetric S_2N stretching).

PVBTA-TFSI Coated NCM and PVBTA-TFSI Coated Vapor Grown Carbon Fibers: For PVBTA-TFSI coated NCM, Mini Spray Dryer B-290 from BUCHI was used to coat PVBTA-TFSI on NCM, as shown in Figure 1. 0.1 g (5 wt% with respect to NCM) or 0.02 g (1 wt% with respect to NCM) of polymer was mixed with 2 g of NCM and 30 g of acetone as the precursor suspension. The mixing step was conducted by vigorous stirring and takes 1 h to make sure the particle aggregation was broken into a smaller size. The inlet temperature was 150 $^\circ\text{C}$, the volume flow (i.e., suction of vacuum pump) was 37 m^3 h^{-1} , the feed rate of polymer solution was 8 mL min^{-1} , and the N_2 flow was 40 L min^{-1} . The spray drying condition was optimized to get the highest productivity of ≈ 50 – 70 wt%. Additionally, the 5 wt% PVBTA-TFSI coated NCM and 1 wt% PVBTA-TFSI coated NCM were noted as 5P-NCM and 1P-NCM, respectively, based on the NCM-polymer ratio of the precursor suspension. Finally, coated NCM was dried in vacuum at 80 $^\circ\text{C}$ for 48 h.

For PVBTA-TFSI coated VGCF, a precursor was prepared by dissolving 20 mg of PVBTA-TFSI polymer in 40 mL acetone. To create a carbon composite, 100 mg of VGCF was sonicated in 20 mL of acetone and then added dropwise to the PVBTA-TFSI polymer solution. The resulting dispersion was then ultrasonicated for 30 min and stirred overnight at room temperature to achieve a homogeneous solution. Next, the coated VGCF was vacuum filtered, washed with 20 mL of acetone, and dried in a vacuum oven at 80 $^\circ\text{C}$.

X-Ray Diffraction: XRD was used to characterize PVBTA-TFSI and check the chemical stability between PVBTA-TFSI or LiTFSI and LPSCI by using Panalytical Empyrean XRD with $\text{Cu K}\alpha$ radiation. Diffraction patterns were collected in a 2θ angular range from 10 $^\circ$ to 85 $^\circ$ with a step size of 0.026 $^\circ$, 0.04 rad. soller slits, and 1/2 $^\circ$ anti-scatter slit. To check the chemical stability between PVBTA-TFSI or LiTFSI with LPSCI, PVBTA-TFSI or LiTFSI were mixed with LPSCI in a weight ratio of 1:1 (≈ 500 mg in total) by grinding in an agate mortar and then pressed into pellets (8 mm in diameter). After that, the pellets were heated and maintained at 80 $^\circ\text{C}$ for 24 h, followed by a grinding process in the agate mortar to turn pellets into powder. Finally, the powder after heating was characterized by XRD.

Thermogravimetric Analysis: TGA measurements were conducted with ≈ 20 mg of samples by STA 409 PC (Netzsch-Gerätebau GmbH) at the temperature ranging from 25 to 1000 $^\circ\text{C}$, under air with a heating rate of 10 $^\circ\text{C min}^{-1}$.

^1H Nuclear Magnetic Resonance: Bruker Avance II recorded the ^1H NMR spectra of PVBTA-TFSI at 400 MHz in deuterated acetone. The chemical shifts were recorded by parts per million (ppm). Tetramethylsilane was used as the internal reference for analysis.

Fourier-Transform Infrared Spectroscopy: FT-IR spectra of PVBTA-TFSI, PVBTA-Cl, and LiTFSI were recorded with a total number of 96 scans on an ATR-FTIR Thermo Fischer Scientific iD5 ATR spectrometer (550–4000 cm^{-1}). To check the chemical stability between PVBTA-TFSI or LiTFSI with LPSCI, PVBTA-TFSI or LiTFSI was mixed with LPSCI in the agate mortar and then pressed to pellets. Subsequently, the pellets were heated and

maintained at 80 °C for 24 h. FT-IR spectra were measured in pellet form before and after the heating process.

Brunauer–Emmett–Teller Analysis: Specific surface area calculations of PVbTA-TFSI coated and pristine NCMs were measured by the BET method. Before measurements, the samples were evacuated at 120 °C for 12 h in standard glass tubes. BET measurements were performed at an automated gas adsorption station (Autosorb-1-MP, Quantachrome Instruments) at 77 K maintained by liquid nitrogen in standard cryostats.

Scanning Electron Microscopy: SEM (Merlin, Zeiss) at an accelerating voltage of 3 kV and accelerating current of 200 pA was adopted to characterize the morphology of NCMs. Back-scattered electron images and secondary electron images were recorded. For sample preparation, polymer coatings and pristine NCMs were measured in powder form, sticking tightly on the conductive carbon tape.

Focused-Ion Beam Scanning Electron Microscopy: The cross-section of coated and pristine NCM powders and cathode composite pellets were analyzed using a XEIA Xe-plasma FIB (TESCAN). For sample preparation, FIB craters were milled in a low-angle condition with a 1 nA Xe-ion beam without any polished step under –135 °C maintained by liquid nitrogen. After that, back-scattered electron images and secondary electron images were recorded at an acceleration voltage of 3 kV and acceleration current of 200 pA.

Energy-Dispersive X-Ray Spectroscopy: After SEM or FIB-SEM measurements, energy-dispersive X-ray spectroscopy (X-Max-Extreme detector, Oxford Instruments) was adopted to characterize the coating layer on NCM. However, to get signals that are more precise from EDX, the accelerating voltage and current were raised to 5 kV and 2 nA, respectively. Additionally, the working distance was controlled at 5.5–5.6 mm. Elements for EDX analysis: C, N, O, F, S, Mn, Co, Ni.

Transmission Electron Microscopy: As the polymer is mainly made of the light element carbon, whereas NCM consisted of heavier transition metals, the materials exhibited a different contrast in TEM bright field images. These images were recorded with a TVIPS TEMCam XF416FS camera on a JEOL JEM-3010 microscope at 300 kV acceleration voltage. For this purpose, powder of uncoated or coated NCM particles was sprinkled on a holey carbon copper TEM grid. Loose powder was removed by evacuating the TEM holder in a pumping stand before transferring it to the TEM to preserve the TEM vacuum.

Time-Of-Flight Secondary Ion Mass Spectrometry: ToF-SIMS was performed using a M6 Hybrid SIMS (IONTOF GmbH) equipped with a 30 kV Bi-cluster primary ion gun for analysis and a 20 kV argon gas cluster source (GCIB) for depth profiling. The GCIB was highly suitable for organic-inorganic composite materials.^[76,77] Charged fragments were obtained as a result of a collision cascade caused by the impact of the high-energy primary ion beam during ToF-SIMS measurements. All samples were prepared in a glovebox, attached to the sample holder using non-conductive adhesive tape and transferred to the SIMS instrument using the LEICA EM VCT500 shuttle (Leica Microsystems). Pristine and coated NCM materials were investigated. Furthermore, pristine (before cycling) and cycled (after cycling) composite cathodes were compared with uncoated and coated NCM after removal of the stainless-steel current collector. To ensure comparability, all samples were prepared in the same way and under the same conditions. For analysis, the instrument is operated in the spectrometry mode using Bi_3^+ as primary ions (0.60 pA) in the negative mode, which provides high mass resolution (full width at half maximum $m/\Delta m > 15\,000$ @ $m/z = 62.97$ (PO_2^-)). The analysis area was set to $100 \times 100 \mu\text{m}^2$, which was rasterized with 128×128 pixels and a primary ion dose of 1.0×10^{12} ions cm^{-2} . To ensure sufficient statistical sampling and reliability of the results, 10 mass spectra were measured per sample. For sputtering, Ar_{1500}^+ clusters were used (5 kV, 5 nA, $300 \times 300 \mu\text{m}^2$). The interlaced sputter mode was done with 3 s sputtering followed by scanning the $150 \times 150 \mu\text{m}^2$ field with 128×128 pixels. The evaluation of the ToF-SIMS data was performed with the software SurfaceLab 7.2 (IONTOF GmbH).

Electrode Composite and Cell Assembly: All of the cell tests were performed with a pellet-type cell casing inside an argon-filled glovebox (Lab-Master, MBraun, Garching, Germany, <0.1 ppm of O_2 , <0.1 ppm of H_2O). Asymmetric cells for electrochemical analysis except cyclic voltammetry

were prepared: InLi | LPSCI | LPSCI, VGCF, NCM. First, 80 mg of LPSCI as a separator were pressed into a pellet within the peek cylinder insulator. Next, the cathode composite was made by mixing 70 wt% of pristine or coated NCM, 30 wt% of LPSCI, and an additional 1 wt% of VGCF in an agate mortar for ≈ 20 min. Then 12 mg of cathode composite was pressed on one side of the electrolyte. Finally, indium (100 μm thickness and 9 mm in diameter) and lithium foils (125 μm thickness and 6 mm in diameter) were pressed on the other side as the anode. After cell assembly, the whole stack of the cell was pressed under 30 kN for 3 min, resulting in $\approx 400 \mu\text{m}$ solid electrolyte with $\approx 30 \mu\text{m}$ cathode composite. Before electrochemical analysis, the whole cell was placed in an external aluminum framework (≈ 50 MPa). Details of the cell assembly were also depicted as a cross-section figure shown in Figure S17, Supporting Information.

For cyclic voltammetry, asymmetric cells of the following setup were prepared: InLi | LPSCI | LPSCI, carbon fibers. To prepare 100 mg of cathode composite, 9.09 mg of VGCF is added to 90.90 mg LPSCI, and mortared for 15 min. To prepare the cell for analysis, 80 mg of LPSCI were pressed into a pellet as a separator within the PEEK cylinder insulator. 30 mg of LPSCI-carbon fiber composite was pressed on one side of the electrolyte. Finally, indium (100 μm thickness and 9 mm in diameter) and lithium foils (125 μm thickness and 6 mm in diameter) were pressed on the other side as the anode. After cell assembly, the whole stack of the cell was pressed under 30 kN for 3 min. Before electrochemical analysis, the whole cell was placed in an external aluminum framework (≈ 50 MPa).

Electrochemical Analysis: Batteries were charged and discharged within the voltage window between 2.0 and 3.7 V (vs $\text{Li}^+/\text{Li-In}$) at 25 °C for cycling stability, chronoamperometry, and EIS. The cycling stability was performed at MACCOR electrochemical workstation. Additionally, EIS and chronoamperometry were conducted by VMP-300 (BioLogic) electrochemical workstation. The whole procedure was also shown in Figure S18, Supporting Information. The cycling test adopts two different currents, 0.1 and 0.25 C, however, the EIS measurements were conducted at 0.1 C. Initially, batteries were charged to 3.15 V (vs $\text{Li}^+/\text{Li-In}$), and then chronoamperometry was maintained at 3.15 V (vs $\text{Li}^+/\text{Li-In}$) until the current drops to less than 1% of charging current. After that, EIS was measured right after chronoamperometry at 3.15 V (vs $\text{Li}^+/\text{Li-In}$) from 1 MHz to 100 μHz . The sinusoidal amplitudes of EIS were applied as 10 mV for 1 MHz to 10 mHz; 5 mV for 10 mHz to 1 mHz; and 3 mV for 1 mHz to 100 μHz . The 0.25 C cycle stability runs 200 cycles, and the impedance was measured at the first, second, 53rd, 104th, 155th, and 206th cycles under 0.1 C at 3.15 V, as shown in Figure S12, Supporting Information. The 0.1 C cycle stability runs for 100 cycles, and the impedance is measured at first to fifth, 10th, 30th, 50th, and 100th cycles under 0.1 C at 3.15 V, as shown in Figure 4. The fitting of the impedance data follows the previous study by using the model as shown in Figure S14, Supporting Information. The low-frequency part was fitted by the finite-space Warburg impedance (Z_{W}).^[8]

Cyclic voltammetry experiments were conducted with a VMP-300 Bio-logic potentiostat at 25 °C. Before the measurement, the cells were maintained at open circuit voltage for 3 h. The cyclic voltammetry measurements used a two-electrode configuration with the anode acting as the reference electrode. First, the voltage sweep was initiated from open circuit voltage to 4 V versus the reference electrode at a scan rate of 1 mV s^{-1} for the oxidative sweep, and then the sweep was reversed until 0 V before returning to the starting potential.

Supporting Information

Supporting Information is available from the Wiley Online Library or from the author.

Acknowledgements

B.X.S., S.S., and F.H.R. acknowledge financial support from the German Federal Ministry of Education and Research (BMBF) for funding via the project FLiPS (03XP0261). Y.Y., T.D., R.R., K.V., and A.H. thank the funding from the BMBF in the framework of the FestBatt cluster of competence

(03XP0433C, 03XP0433D). A.H. is very grateful for funding from the BMBF Professorinnenprogramm III. In addition, the authors are very grateful to Dr. Rafael Meinusch and Prof. Bernd Smarsly for their help with nitrogen physisorption and TGA measurements.

Open access funding enabled and organized by Projekt DEAL.

Conflict of Interest

The authors declare no conflict of interest.

Author Contributions

B.X.S. carried out the syntheses, electrochemical analyses and general materials characterization. Y.Y. performed the TOF-SIMS analysis and T.D. carried out the TEM experiments. S.S., R.R., K.V., A.H., and F.H.R. helped with the analysis and discussion of experimental data. B.X.S., S.S., and F.H.R. conceived the idea and prepared the manuscript. All authors participated in the analysis of the experimental results and contributed to the manuscript.

Data Availability Statement

The data that support the findings of this study are available from the corresponding author upon reasonable request.

Keywords

high-nickel ternary cathode materials, interface degradation, polyelectrolyte, polymer coating, solid electrolytes, solid-state batteries

Received: January 31, 2023

Revised: March 21, 2023

Published online: May 10, 2023

- [1] J. Schnell, T. Günther, T. Knoche, C. Vieider, L. Köhler, A. Just, M. Keller, S. Passerini, G. Reinhard, *J. Power Sources* **2018**, *382*, 160.
- [2] S. Randau, D. A. Weber, O. Kötz, R. Koerver, P. Braun, A. Weber, E. Ivers-Tiffée, T. Adermann, J. Kulisch, W. G. Zeier, F. H. Richter, J. Janek, *Nat. Energy* **2020**, *5*, 259.
- [3] S. Dühnen, J. Betz, M. Kolek, R. Schmuck, M. Winter, T. Placke, *Small Methods* **2020**, *4*, 2000039.
- [4] S.-K. Jung, H. Gwon, S.-S. Lee, H. Kim, J. C. Lee, J. G. Chung, S. Y. Park, Y. Aihara, D. Im, *J. Mater. Chem. A* **2019**, *7*, 22967.
- [5] J. Auvergniot, A. Cassel, J.-B. Ledeuil, V. Viallet, V. Seznec, R. Dedryvère, *Chem. Mater.* **2017**, *29*, 3883.
- [6] D. H. S. Tan, E. A. Wu, H. Nguyen, Z. Chen, M. A. T. Marple, J.-M. Doux, X. Wang, H. Yang, A. Banerjee, Y. S. Meng, *ACS Energy Lett.* **2019**, *4*, 2418.
- [7] G. F. Dewald, S. Ohno, M. A. Kraft, R. Koerver, P. Till, N. M. Vargas-Barbosa, J. Janek, W. G. Zeier, *Chem. Mater.* **2019**, *31*, 8328.
- [8] G. Conforto, R. Ruess, D. Schröder, E. Trevisanello, R. Fantin, F. H. Richter, J. Janek, *J. Electrochem. Soc.* **2021**, *168*, 070546.
- [9] N. Y. Kim, T. Yim, J. H. Song, J.-S. Yu, Z. Lee, *J. Power Sources* **2016**, *307*, 641.
- [10] H. Zhang, H. Liu, L. F. J. Piper, M. S. Whittingham, G. Zhou, *Chem. Rev.* **2022**, *122*, 5641.
- [11] F. Walther, R. Koerver, T. Fuchs, S. Ohno, J. Sann, M. Rohnke, W. G. Zeier, J. Janek, *Chem. Mater.* **2019**, *31*, 3745.
- [12] T.-T. Zuo, R. Rueß, R. Pan, F. Walther, M. Rohnke, S. Hori, R. Kanno, D. Schröder, J. Janek, *Nat. Commun.* **2021**, *12*, 6669.
- [13] T. Bartsch, F. Strauss, T. Hatsukade, A. Schiele, A. Y. Kim, P. Hartmann, J. Janek, T. Brezesinski, *ACS Energy Lett.* **2018**, *3*, 2539.
- [14] S. H. Jung, U.-H. Kim, J.-H. Kim, S. Jun, C. S. Yoon, Y. S. Jung, Y.-K. Sun, *Adv. Energy Mater.* **2020**, *10*, 1903360.
- [15] J.-M. Lim, T. Hwang, D. Kim, M.-S. Park, K. Cho, M. Cho, *Sci. Rep.* **2017**, *7*, 39669.
- [16] E. Trevisanello, R. Ruess, G. Conforto, F. H. Richter, J. Janek, *Adv. Energy Mater.* **2021**, *11*, 2003400.
- [17] Y. Han, S. H. Jung, H. Kwak, S. Jun, H. H. Kwak, J. H. Lee, S.-T. Hong, Y. S. Jung, *Adv. Energy Mater.* **2021**, *11*, 2100126.
- [18] H.-H. Ryu, B. Namkoong, J.-H. Kim, I. Belharouak, C. S. Yoon, Y.-K. Sun, *ACS Energy Lett.* **2021**, *6*, 2726.
- [19] R. Ruess, S. Schweidler, H. Hemmelmann, G. Conforto, A. Bielefeld, D. A. Weber, J. Sann, M. T. Elm, J. Janek, *J. Electrochem. Soc.* **2020**, *167*, 100532.
- [20] U. Nisar, N. Muralidharan, R. Essehli, R. Amin, I. Belharouak, *Energy Storage Mater.* **2021**, *38*, 309.
- [21] D. Kitsche, Y. Tang, Y. Ma, D. Goonetilleke, J. Sann, F. Walther, M. Bianchini, J. Janek, T. Brezesinski, *ACS Appl. Energy Mater.* **2021**, *4*, 7338.
- [22] Y. Lei, J. Ni, Z. Hu, Z. Wang, F. Gui, B. Li, P. Ming, C. Zhang, Y. Elias, D. Aurbach, Q. Xiao, *Adv. Energy Mater.* **2020**, *10*, 2002506.
- [23] F. Walther, F. Strauss, X. Wu, B. Mogwitz, J. Hertle, J. Sann, M. Rohnke, T. Brezesinski, J. Janek, *Chem. Mater.* **2021**, *33*, 2110.
- [24] A. Y. Kim, F. Strauss, T. Bartsch, J. H. Teo, T. Hatsukade, A. Mazilkin, J. Janek, P. Hartmann, T. Brezesinski, *Chem. Mater.* **2019**, *31*, 9664.
- [25] Y.-J. Kim, R. Rajagopal, S. Kang, K.-S. Ryu, *Chem. Eng. J.* **2020**, *386*, 123975.
- [26] D. Kitsche, F. Strauss, Y. Tang, N. Bartnick, A.-Y. Kim, Y. Ma, C. Kübel, J. Janek, T. Brezesinski, *Batteries Supercaps* **2022**, *5*, 202100397.
- [27] R. S. Negi, Y. Yusim, R. Pan, S. Ahmed, K. Volz, R. Takata, F. Schmidt, A. Henss, M. T. Elm, *Adv. Mater. Interfaces* **2022**, *9*, 2101428.
- [28] Y.-Q. Zhang, Y. Tian, Y. Xiao, L. J. Miara, Y. Aihara, T. Tsujimura, T. Shi, M. C. Scott, G. Ceder, *Adv. Energy Mater.* **2020**, *10*, 1903778.
- [29] F. Strauss, J. H. Teo, J. Maibach, A. Y. Kim, A. Mazilkin, J. Janek, T. Brezesinski, *ACS Appl. Mater. Interfaces* **2020**, *12*, 57146.
- [30] R. S. Negi, P. Minnmann, R. Pan, S. Ahmed, M. J. Herzog, K. Volz, R. Takata, F. Schmidt, J. Janek, M. T. Elm, *Chem. Mater.* **2021**, *33*, 6713.
- [31] S. H. Jung, K. Oh, Y. J. Nam, D. Y. Oh, P. Brüner, K. Kang, Y. S. Jung, *Chem. Mater.* **2018**, *30*, 8190.
- [32] E. A. Wu, C. Jo, D. H. S. Tan, M. Zhang, J.-M. Doux, Y.-T. Chen, G. Deysheer, Y. S. Meng, *J. Electrochem. Soc.* **2020**, *167*, 130516.
- [33] J. S. Kim, S. Jung, H. Kwak, Y. Han, S. Kim, J. Lim, Y. M. Lee, Y. S. Jung, *Energy Storage Mater.* **2023**, *55*, 193.
- [34] S. Sen, E. Trevisanello, E. Niemöller, B.-X. Shi, F. J. Simon, F. H. Richter, *J. Mater. Chem. A* **2021**, *9*, 18701.
- [35] Q. Gan, N. Qin, Y. Zhu, Z. Huang, F. Zhang, S. Gu, J. Xie, K. Zhang, L. Lu, Z. Lu, *ACS Appl. Mater. Interfaces* **2019**, *11*, 12594.
- [36] S. P. Culver, R. Koerver, W. G. Zeier, J. Janek, *Adv. Energy Mater.* **2019**, *9*, 1900626.
- [37] A. Sakuda, A. Hayashi, M. Tatsumisago, *Curr. Opin. Electrochem.* **2017**, *6*, 108.
- [38] S. Deng, Y. Sun, X. Li, Z. Ren, J. Liang, K. Doyle-Davis, J. Liang, W. Li, M. N. Banis, Q. Sun, R. Li, Y. Hu, H. Huang, L. Zhang, S. Lu, J. Luo, X. Sun, *ACS Energy Lett.* **2020**, *5*, 1243.
- [39] G.-L. Xu, Q. Liu, K. K. S. Lau, Y. Liu, X. Liu, H. Gao, X. Zhou, M. Zhuang, Y. Ren, J. Li, M. Shao, M. Ouyang, F. Pan, Z. Chen, K. Amine, G. Chen, *Nat. Energy* **2019**, *4*, 484.
- [40] Y. Huang, J. Xia, G. Hu, Y. Cao, Z. Peng, J. Fan, Y. Tao, T. Li, Z. Zhang, Z. Xue, K. Du, *Electrochim. Acta* **2020**, *332*, 135505.
- [41] Y. Cao, X. Qi, K. Hu, Y. Wang, Z. Gan, Y. Li, G. Hu, Z. Peng, K. Du, *ACS Appl. Mater. Interfaces* **2018**, *10*, 18270.
- [42] E.-H. Lee, J.-H. Park, J.-H. Cho, S.-J. Cho, D. W. Kim, H. Dan, Y. Kang, S.-Y. Lee, *J. Power Sources* **2013**, *244*, 389.

- [43] H. Wang, J. Lin, X. Zhang, L. Wang, J. Yang, E. Fan, F. Wu, R. Chen, L. Li, *ACS Appl. Energy Mater.* **2021**, *4*, 6205.
- [44] Y.-S. Lee, W.-K. Shin, A. G. Kannan, S. M. Koo, D.-W. Kim, *ACS Appl. Mater. Interfaces* **2015**, *7*, 13944.
- [45] S. H. Ju, I.-S. Kang, Y.-S. Lee, W.-K. Shin, S. Kim, K. Shin, D.-W. Kim, *ACS Appl. Mater. Interfaces* **2014**, *6*, 2546.
- [46] A. Yiğitalp, A. Taşdemir, S. Alkan Gürsel, A. Yürüm, *Energy Storage* **2020**, *2*, e154.
- [47] D. Becker, M. Börner, A. Friesen, S. Klein, U. Rodehorst, M. Diehl, M. Winter, T. Placke, R. Schmich, *J. Electrochem. Soc.* **2020**, *167*, 060524.
- [48] B. Li, G. Li, D. Zhang, J. Fan, D. Chen, Y. Ge, F. Lin, C. Zheng, L. Li, *ChemistrySelect* **2019**, *4*, 6354.
- [49] S. Vauthier, M. Alvarez-Tirado, G. Guzmán-González, L. C. Tomé, S. Cotte, L. Castro, A. Guéguen, D. Mecerreyes, N. Casado, *Mater. Today Chem.* **2023**, *27*, 101293.
- [50] T. A. Ha, H. Li, X. Wang, L. A. O'Dell, M. Forsyth, C. Pozo-Gonzalo, P. C. Howlett, *ACS Appl. Energy Mater.* **2021**, *4*, 434.
- [51] N. G. Hoogeveen, C. W. Hoogendam, R. Tuinier, M. A. Cohen Stuart, *Int. J. Polym. Anal. Charact.* **1995**, *1*, 315.
- [52] C. Willa, J. Yuan, M. Niederberger, D. Koziej, *Adv. Funct. Mater.* **2015**, *25*, 2537.
- [53] B. B. Patel, J. K. Patel, S. Chakraborty, *Recent Pat. Drug Delivery Formulation* **2014**, *8*, 63.
- [54] L. S. C. Wan, P. W. S. Heng, C. G. H. Chia, *Int. J. Pharm.* **1991**, *77*, 183.
- [55] W. I. J. Kariuki, B. Freireich, R. M. Smith, M. Rhodes, K. P. Hapgood, *Chem. Eng. Sci.* **2013**, *92*, 134.
- [56] Y. Zhou, Z. Hu, Y. Huang, Y. Wu, Z. Hong, *J. Alloys Compd.* **2021**, *888*, 161584.
- [57] D. Nikolaeva, I. Azcune, E. Sheridan, M. Sandru, A. Genua, M. Tanczyk, M. Jaschik, K. Warmuzinski, J. C. Jansen, I. F. J. Vankelecom, *J. Mater. Chem. A* **2017**, *5*, 19808.
- [58] M. Li, L. Wang, B. Yang, T. Du, Y. Zhang, *Electrochim. Acta* **2014**, *123*, 296.
- [59] A. Priebe, T. Xie, G. Bürki, L. Pethö, J. Michler, *J. Anal. At. Spectrom.* **2020**, *35*, 1156.
- [60] S. Randau, F. Walther, A. Neumann, Y. Schneider, R. S. Negi, B. Mogwitz, J. Sann, K. Becker-Steinberger, T. Danner, S. Hein, A. Latz, F. H. Richter, J. Janek, *Chem. Mater.* **2021**, *33*, 1380.
- [61] K. J. Kim, M. Balaish, M. Wadaguchi, L. Kong, J. L. M. Rupp, *Adv. Energy Mater.* **2021**, *11*, 2002689.
- [62] K. Ishidzu, Y. Oka, T. Nakamura, *Solid State Ionics* **2016**, *288*, 176.
- [63] R. Koerver, W. Zhang, L. de Biasi, S. Schweidler, A. O. Kondrakov, S. Kolling, T. Brezesinski, P. Hartmann, W. G. Zeier, J. Janek, *Energy Environ. Sci.* **2018**, *11*, 2142.
- [64] R. Koerver, I. Aygün, T. Leichtweiß, C. Dietrich, W. Zhang, J. O. Binder, P. Hartmann, W. G. Zeier, J. Janek, *Chem. Mater.* **2017**, *29*, 5574.
- [65] P. Li, Y. Zhao, Y. Shen, S.-H. Bo, *J. Phys. Condens. Matter* **2020**, *2*, 022002.
- [66] J. Zhang, C. Zheng, L. Li, Y. Xia, H. Huang, Y. Gan, C. Liang, X. He, X. Tao, W. Zhang, *Adv. Energy Mater.* **2020**, *10*, 1903311.
- [67] I. Kochetkov, T.-T. Zuo, R. Ruess, B. Singh, L. Zhou, K. Kaup, J. Janek, L. Nazar, *Energy Environ. Sci.* **2022**, *15*, 3933.
- [68] J. Song, M. Z. Bazant, *J. Electrochem. Soc.* **2012**, *160*, A15.
- [69] M. Doyle, J. Newman, *J. Appl. Electrochem.* **1997**, *27*, 846.
- [70] C. J. Wen, B. A. Boukamp, R. A. Huggins, W. Weppner, *J. Electrochem. Soc.* **1979**, *126*, 2258.
- [71] S. Wang, X. Zhang, S. Liu, C. Xin, C. Xue, F. Richter, L. Li, L. Fan, Y. Lin, Y. Shen, J. Janek, C.-W. Nan, *J. Materiomics* **2020**, *6*, 70.
- [72] J. Zhang, H. Zhong, C. Zheng, Y. Xia, C. Liang, H. Huang, Y. Gan, X. Tao, W. Zhang, *J. Power Sources* **2018**, *391*, 73.
- [73] H. Li, A. Liu, N. Zhang, Y. Wang, S. Yin, H. Wu, J. R. Dahn, *Chem. Mater.* **2019**, *31*, 7574.
- [74] F. Walther, S. Randau, Y. Schneider, J. Sann, M. Rohnke, F. H. Richter, W. G. Zeier, J. Janek, *Chem. Mater.* **2020**, *32*, 6123.
- [75] J. C. Vickerman, *Molecular Surface Mass Spectrometry by SIMS*, Wiley, New Jersey, USA **2009**.
- [76] D. Rading, R. Moellers, H.-G. Cramer, E. Niehuis, *Surf. Interface Anal.* **2013**, *45*, 171.
- [77] S. Rabbani, A. M. Barber, J. S. Fletcher, N. P. Lockyer, J. C. Vickerman, *Anal. Chem.* **2011**, *83*, 3793.